Influence of stimulated Raman scattering on Kerr domain walls and localized structures

P. Parra-Rivas [1], S. Coulibaly [2], M. G. Clerc [3] and M. Tlidi [4]

[1] *OPERA-photonique, Université libre de Bruxelles, 50 Avenue F. D. Roosevelt, CP 194/5, B-1050 Bruxelles, Belgium*

[2] *Université de Lille, CNRS, UMR 8523-PhLAM-Physique des Lasers Atomes et Molécules, F-59000 Lille, France*

[3] *Departamento de Física and Millennium Institute for Research in Optics, Facultad de Ciencias Físicas y Matemáticas, Universidad de Chile, Casilla 487-3, Santiago, Chile*

[4] *Faculté des Sciences, Université Libre de Bruxelles, CP 231, Campus Plaine, B-1050 Bruxelles, Belgium*

(Received 7 July 2020; accepted 11 December 2020; published 7 January 2021)

We investigate the influence of the stimulated Raman scattering on the formation of bright and dark localized states in all-fiber resonators subject to a coherent optical injection, when operating in the normal dispersion regime. In the absence of the Raman effect, and far from any modulational instability, localized structures form due to the locking of domain walls connecting two coexisting continuous wave states, and undergo a particular bifurcation structure known as collapsed snaking. The stimulated Raman scattering breaks the reflection symmetry of the system, and modifies the dynamics, stability, and locking of domain walls. This modification leads to the formation of, not only dark, but also bright moving localized states, which otherwise are absent. We perform a detailed bifurcation analysis of these localized states, and classify their dynamics and stability as a function of the main parameters of the system.

DOI: 10.1103/PhysRevA.103.013507

I. INTRODUCTION

Dissipative localized structures (LSs), also known as *dissipative solitons*, are coherent states emerging in extended systems far from the thermodynamic equilibrium [1–5]. Dissipative LSs may appear in a large variety of pattern forming systems ranging from fluid mechanics and optics, to biology and plant ecology [3–10]. These robust states can behave like discrete objects in continuous systems, and can display a variety of different dynamics such as periodic oscillations, chaos, or excitability [4,5]. LSs evolve on macroscopic spatial scales, and can be only maintained by permanent nonequilibrium constraints. Furthermore, once the system parameters are fixed, they are unique, and hence different from the well-known conservative solitons that appear as one-parameter families [3,4]. The formation of LSs is usually related with the presence of bistability between different coexisting steady states, and therefore a LS can be seen as a portion of one of those states embedded on the other one [11].

Classic examples of dissipative systems where LSs may emerge are found in the field of nonlinear optics and laser physics [3–5]. In this context, LSs have been widely studied in externally driven diffractive nonlinear cavities with cubic (i.e., Kerr) nonlinearities [12–15]. In these types of cavities, two-dimensional LSs, consisting in spots of light embedded on a homogeneous background, form in the transverse plane to the propagation direction, and are commonly known as *spatial cavity solitons*. Similar types of LSs have been shown in wave-guided dispersive Kerr cavities, where they correspond to one-dimensional *temporal cavity solitons* emerging along the propagation direction [16–20]. Temporal LSs have been considered as the basis for all-optical buffering [16], and in the last decade, for broadband frequency comb generation in microresonators [21–23]. In both, diffractive and dispersive Kerr cavities, LSs emerge from a double balance between Kerr nonlinearity and spatial coupling (e.g., diffraction and/or dispersion) on one hand, and energy gain and losses on the other hand [3].

In dispersive Kerr cavities, temporal LSs can form in either the normal or anomalous dispersion regimes. In the normal regime, LSs arise due to the locking of domain walls (DWs), also known as switching waves or fronts, connecting two different continuous-wave (CW) states [19,20,24–26]. These LSs are different from those appearing in the anomalous regime, whose formation is related with the heteroclinic tangle of coexisting CW states and subcritical Turing patterns [16,17,27–29].

Close to the zero-dispersion wavelength, the influence of high-order effects, such as third- and fourth-order dispersion, has to be considered. These terms may cause important modifications on the LS dynamics, such as the stabilization of different types of LSs, in both normal and anomalous regimes [30–35].

In systems made of amorphous materials, such as optical fibers, stimulated Raman scattering (SRS), originated from the delayed material response to electromagnetic excitation, may also have important implications on the LSs dynamics. These implications have been studied by many authors in the context of the anomalous dispersion regime, where most of the studies focus on the cavity soliton dynamics and stability [36–41].

In normal dispersion materials, the influence of SRS on the dynamics of DWs and LSs has also attracted an important attention in the last years [42–45]. In particular, it has

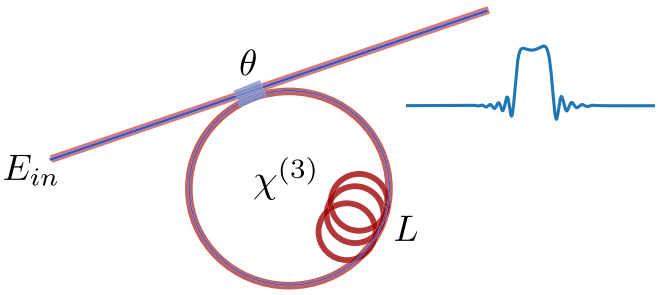

FIG. 1. Sketch of an all-fiber cavity of length L driven by an external laser beam of amplitude $E_{\rm in}$ through a beam splitter with intensity transmission coefficient θ. Dissipative structures of different type form and circulate along the cavity.

been shown that SRS may stabilize moving bright LSs, which are absent otherwise [43,45]. Close to the nascent bistability onset, where the system can be described by a real order parameter equation, the DWs interaction and locking has been theoretically analyzed, and the bifurcation structure of the resulting LSs has been studied [43,45]. However, such description is only valid near that point, and an extension of the analysis to the whole parameter space is required. The aim of this article is to unveil the implications that SRS may have on the dynamics and bifurcation structure of the DWs and LSs arising in these systems.

The paper is organized as follows. In Sec. II, we introduce the model describing dispersive Kerr cavities in the presence of SRS. Section III focuses on the CW states and the formation of DWs. Later in Sec. IV, we introduce the mechanism of DWs locking for the formation of LSs, and we study their bifurcation structure in the absence of SRS. In Sec. V, we analyze the modification of the previous scenario when SRS is considered and how the SRS affects the formation of LSs. Sections VI and VII are devoted to the bifurcation and stability analysis of the Raman LSs. Here we classify the different dynamical regimes in terms of the main parameters of the system. Finally, in Sec. VIII, a short discussion and the main conclusions of our work are given.

II. THE LUGIATO-LEFEVER MODEL WITH STIMULATED RAMAN SCATTERING

We consider an all-fiber cavity of length L driven by a coherent injected field of amplitude $E_{\rm in}$ as shown in Fig. 1, where θ represents the intensity transmission coefficient of the beam splitter. The transmitted part of the injected field circulating within the cavity is affected by Kerr nonlinearity, chromatic dispersion, forcing, and dissipation. In the high-finesse limit, and in the presence of SRS, the intracavity field envelope E of the electric field is described by the extended Lugiato-Lefever equation,

$$t_R\partial_t E = -(\alpha+i\delta_0)E+\sqrt{\theta}E_{\rm in}-i\frac{\beta_2 L}{2}\partial_\tau^2 E+i\gamma L(1-f_R)|E|^2E + if_R L\gamma E\int_0^\infty R(\tau')|E(\tau-\tau')|^2d\tau', \quad (1)$$

where τ is the fast time, t is the slow time, t_R is the round-trip time, γ is the nonlinear coefficient, β_2 is the chromatic dispersion coefficient, δ_0 is the phase detuning between the pump field and the nearest cavity resonance, and α represents the linear cavity losses [37,46,47].

The nonlocal delay response term models the SRS, and in agreement with experimental measurements, its kernel or influence function takes the form [48],

$$R(\tau)=\frac{\tau_1^2+\tau_2^2}{\tau_1\tau_2^2}e^{-\tau/\tau_2}\sin(\tau/\tau_1), \quad (2)$$

where the parameter f_R denotes the strength of SRS, and the parameters $\tau_{1,2}$ depend on the type of fiber. Note that in real systems, perturbations due to the higher order dispersion effects may be present alongside the SRS. However, in this theoretical study, for simplicity, we neglect those effects, and focus on the SRS.

The LL equation was first derived to describe passive diffractive cavities [46], and later on, in the context of wave-guide dispersive cavities such as fiber cavities [47], whispering gallery mode resonators [49], and integrated ring resonators [22]. This equation has been also derived in the context of left-handed materials [50], for a chain of coupled silver nanoparticles embedded in a glass [51], in coupled-waveguide resonators [52], and for extended Josephson junctions [53].

This model constitutes a paradigm for the study of various dynamical properties of laser fields confined in either diffractive or dispersive nonlinear optical cavities [6] such as the emergence of patterns [12,28,54–56], the formation of LSs and clusters of them [12,15,25,27–29,57–59], self-pulsating LSs or breathers [14,17,25,29], LSs excitability [15], and some other complex spatiotemporal dynamics such as spatiotemporal chaos [17,60,61] and rogue waves [62–65].

Considering the transformations $E=e_cA$, $\tau=\tau_cX$, and $t=t_cT$, Eq. (1) can be written in the dimensionless form,

$$\partial_T A = -(1+i\Delta)A-i\eta_2\partial_X^2A+i(1-f_R)|A|^2A + if_RA(\mathsf{R}\otimes|A|^2)+S, \quad (3)$$

where $e_c=\sqrt{\alpha/\gamma L}$, $\tau_c=\sqrt{L|\beta_2|/2\alpha}$, and $t_c=t_R/\alpha$, and the normalized detuning, pump intensity, and group velocity dispersion coefficients read

$$\Delta=\frac{\delta_0}{\alpha},\quad S=\sqrt{\frac{\theta\gamma L}{\alpha^3}}E_{\rm in},\quad \eta_2=\mathrm{sgn}(\beta_2).$$

In Eq. (3), $\otimes$ is the convolution between the intensity $|A|^2$, and the normalized extended Raman kernel R,

$$\mathsf{R}(X)\equiv\mathsf{H}(X)R'(X)\equiv\mathsf{H}(X)\eta e^{-aX}\sin(bX), \quad (4)$$

where H is the Heaviside function, and

$$\eta=\tau_c\frac{\tau_1^2+\tau_2^2}{\tau_1\tau_2^2},\quad a=\tau_c/\tau_2,\quad b=\tau_c/\tau_1.$$

The SRS term is calculated through the convolution theorem which states

$$\mathsf{R}\otimes|A|^2=\mathcal{F}^{-1}(\mathcal{F}[\mathsf{R}]\cdot\mathcal{F}[|A|^2]),$$

where $\mathcal{F}$ represents the Fourier transform.

The Fourier transform of R reads

$$\mathcal{F}[\mathsf{R}](k)=\frac{\eta b}{b^2+(a-ik)^2}, \quad (5)$$

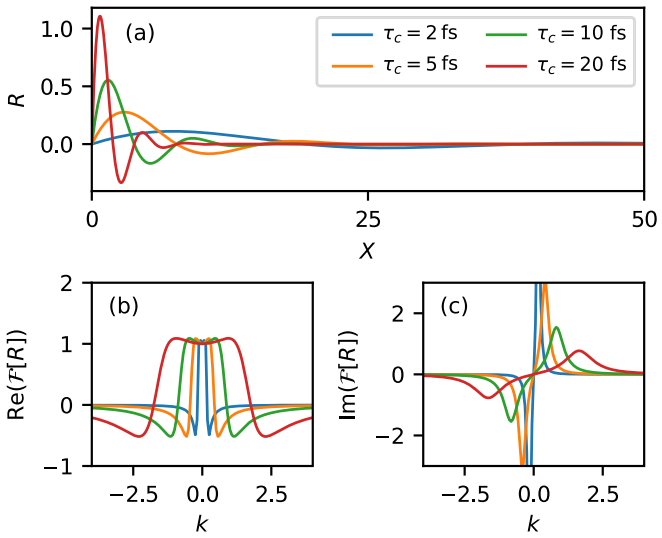

FIG. 2. In (a) the normalized kernel R associated with SRS for different values of the characteristic parameter τ_c. (b) and (c) The real and imaginary parts of $\mathcal{F}[\mathsf{R}]$. Here $(\tau_1, \tau_2, f_R) = (12.2\text{ fs}, 32\text{ fs}, 0.18)$.

and its real and imaginary parts,

$$\mathrm{Re}(\mathcal{F}[\mathsf{R}]) = b\eta(a^2 + b^2 - k^2)/Z(k), \tag{6a}$$

and

$$\mathrm{Im}(\mathcal{F}[\mathsf{R}]) = 2\eta abk/Z(k), \tag{6b}$$

respectively, with $Z(k) = (a^2 + b^2 - k^2)^2 + 4a^2k^2$. The imaginary part of $\mathcal{F}[\mathsf{R}]$ corresponds to the Raman gain spectrum, while the real one represents the modification of the refractive index due to the SRS term [66].

The SRS term introduces an additional dependency on τ_c which becomes an important parameter for controlling the strength of the Raman response function R, and furthermore connects to physical parameters of the cavity such as the chromatic dispersion coefficient, length, and losses [40,43]. The modification of the SRS response with τ_c is plotted in Fig. 2(a) for $\tau_c = 2$, 5, 10, and 20 fs, and $\mathrm{Re}(\mathcal{F}[\mathsf{R}])$ and $\mathrm{Im}(\mathcal{F}[\mathsf{R}])$ are shown in Figs. 2(b) and 2(c), respectively. Decreasing τ_c, the wavelength of R increases, while its envelope decreases [see Fig. 2(a)]. In contrast, when τ_c is very large (i.e., $\tau_c \to \infty$), R becomes very sharp approaching an instantaneous response (i.e., a Dirac delta).

In the absence of SRS, Eq. (3) is invariant under the transformation $X \to -X$ (i.e., X-reflection symmetry), and its LS solutions normally preserve this symmetry. In contrast, when SRS is taken into account, the reflection symmetry is broken, leading to asymmetric solutions which now drift at a constant speed v, which depends on the SRS control parameters [43].

In what follows, we focus on the normal dispersion regime (i.e., $\eta_2 = 1$), and we fix $f_R = 0.18$, $\tau_1 = 12.2$ fs, and $\tau_2 = 32$ fs corresponding to the common parameters of fused-silica-based fibers [48]. With these specifications the main control parameters of the system are Δ, S, and τ_c. Furthermore, in this work we consider a normalized domain length $l = 100$ and periodic boundary conditions.

III. CONTINUOUS WAVE BISTABILITY AND DOMAIN WALLS DYNAMICS

The stationary states (i.e., $\partial_T A = 0$) of this system are described by

$$-(1 + i\Delta)A + v\partial_X A - i\eta_2\partial_X^2 A + i(1 - f_R)|A|^2 A + if_R A(\mathsf{R} \otimes |A|^2) + S = 0, \tag{7}$$

where we have considered the comoving frame transformation $X \to X - vT$, to take into account moving states at constant speed v.

The basic state solutions of Eq. (7) are the homogeneous or CW states A_h satisfying

$$I_h^3 - 2\Delta I_h^2 + (1 + \Delta^2)I_h = S^2, \tag{8}$$

where $I_h \equiv |A_h|^2$. For $\Delta < \sqrt{3}$, A_h is single valued. For $\Delta > \sqrt{3}$, A_h is triple valued, and composed by the three solutions A_b, A_m, and A_t, which are separated by two folds or saddle-node bifurcations $\mathrm{SN}_{t,b}$ occurring at

$$I_{t,b} = \frac{2\Delta}{3} \pm \frac{1}{3}\sqrt{\Delta^2 - 3}. \tag{9}$$

In the later case, A_h shows a hysteresis loop like the one plotted in Fig. 3 (top panel) for $\Delta = 4$. In the absence of SRS ($f_R = 0$), the middle branch A_m is always spatiotemporally unstable, the top one A_t is always stable, and the bottom one A_b undergoes a modulational instability (MI) at $(S_c, I_c) \equiv (\sqrt{1 + (1 - \Delta)^2}, 1)$ such that it is stable for $S < S_c$, and unstable between MI and SN_b. We plot stable (unstable) solution branches using solid (dashed) lines. In the range between SN_t and MI (S_c) (see light shadowed area in Fig. 3) stable A_b and A_t coexist, and in the following we refer to this interval as the *bistability* region.

Within the bistability region, DWs connecting A_b and A_t either upwards (DW_u) or downwards (DW_d) can form (see the inset in Fig. 3). DW_u and DW_d are related by the reflection $X \to -X$ respect to their center, i.e., $\mathrm{DW}_u(X) = \mathrm{DW}_d(-X)$, and in general, are not stationary, but move at constant speed and opposite direction depending on the parameters of the system.

To gain some insight about the DWs behavior let us first show how an initial condition of the form,

$$g^{b(t)}(X) = A_{b(t)} \pm he^{-[X/\sigma]^{10}}, \tag{10}$$

consisting in a super-Gaussian profile sitting on A_h, with σ and h being its standard deviation and height, evolves in time. Figure 3(a) shows the evolution of Eq. (10) for $S = 2.1 < S_M$, and corresponds to the left dashed gray line in the CW diagram. The initial g^b profile establishes a connection between A_b and A_t, leading to the formation of DW_u and DW_d, which soon after move inwards, with the same speed and opposite propagation direction. Eventually, the DWs annihilate one another, bringing the system back to A_b.

Figure 3(b) shows the evolution of the same initial condition for $S = 2.3 > S_M$. For this value, the DWs move outwards, and eventually they meet at the boundaries of the domain, where they collide and disappear, such that the system terminates at the A_t state. The transition between these two scenarios takes place at the Maxwell point S_M of

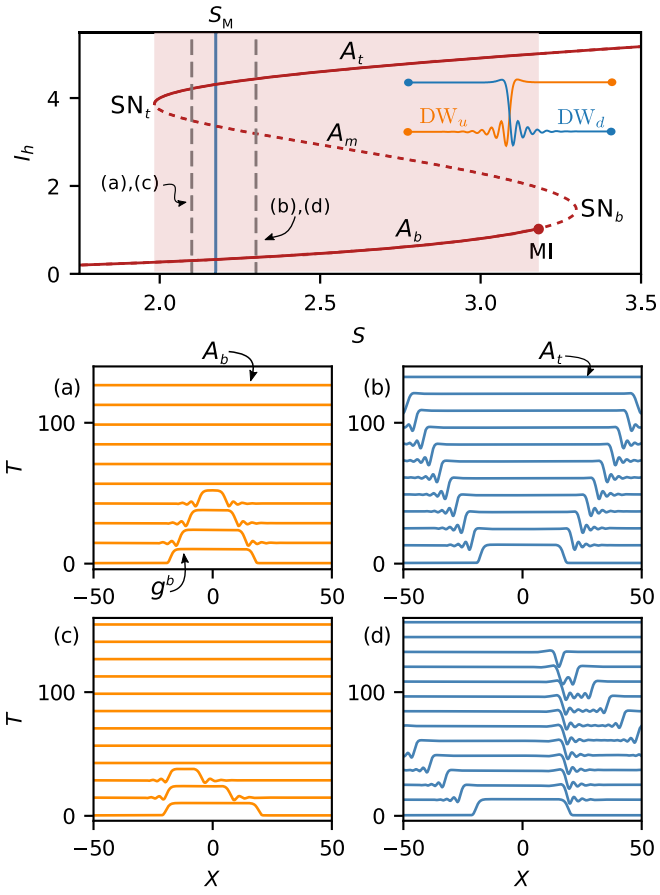

FIG. 3. (Top panel) Intensity of the CW state as a function of S for $\Delta = 4$. Stable (unstable) branches are shown with solid (dashed) lines. The light shadowed area shows the bistability region. The solid blue vertical line marks the Maxwell point of the system S_M, and the two vertical dashed gray lines correspond to the temporal evolutions shown in panels (a)–(d). (a) and (b) The evolution of two different initial conditions of the form g^b in the absence of SRS. (c) and (d) The temporal evolution of the same initial condition in the presence of SRS for $\tau_c = 5$ fs.

the system (see Fig. 3) where the DW speed cancels out [26,67].

When the SRS is taken into account ($f_R \neq 0$), the features and dynamics of DWs change. The SRS breaks the reflection symmetry of the system, and DWs are no more related by the transformation $X \to -X$ [i.e., $\mathrm{DW}_u(X) \neq \mathrm{DW}_d(-X)$]. Due to this asymmetry, DW_u and DW_d now move at different speeds and opposite directions, leading to the asymmetric time evolution shown in Figs. 3(c) and 3(d). For $S = 2.1$ [see Fig. 3(c)] DW_u moves slower than DW_d, although they eventually collide bringing the system back to A_b. For $S = 2.3$ [see Fig. 3(d)], DW_u moves much faster than DW_d, but as before, their annihilation eventually takes place, and the system finally reaches A_t.

IV. FORMATION OF LOCALIZED STATES IN THE ABSENCE OF STIMULATED RAMAN SCATTERING

The temporal evolutions shown in Fig. 3 correspond to values of S, far from S_M, where DWs annihilate one another, leading to one of the CW attractors, either A_b or A_t. Close to the Maxwell point S_M, however, DWs may lock at certain separations leading to the formation of LSs of different widths [25,26,43]. In this section, we illustrate this mechanism in the absence of SRS ($f_R = 0$), and later, in Sec. V, we show the implications that the SRS may have on the LSs formation, dynamics, and stability.

A. Locking of domain walls

Close to the Maxwell point S_M [e.g., for $S = 2.18$ in Fig. 3 (top)], two g^t initial conditions of different widths lead to the formation of two coexistent dark LSs like those shown in Figs. 4(a) and 4(b). The formation of these LSs and their coexistence is a well-understood phenomenon mediated by the interaction and locking of DWs [11,25,68,69]. Let us briefly review this mechanism.

In the absence of SRS, $\mathrm{DW}_{u,d}$ profiles look like those shown schematically in Fig. 4(c). These DWs exhibit *monotonic tails* around A_t, and *oscillatory tails* about A_b. These tails can be asymptotically described by $A(X) = A_{b(t)} + \epsilon e^{\lambda X}$, where $\epsilon \ll 1$ and λ is a complex number, solution of the eigenvalue equation [25],

$$\lambda^4 - (4I_h - 2\Delta)\lambda^2 + \Delta^2 + 3I_h^2 - 4\Delta I_h + 1 = 0. \tag{11}$$

Figure 4(c) shows the set of eigenvalues associated with A_b (left) and A_t (right). While the eigenvalues associated with A_t are purely real ($\pm c_1, \pm c_2$), those associated with A_b are complex conjugates ($\pm c_3 \pm i c_4$), where $c_i \in \mathbb{R}$ ($i = 1, \ldots, 4$). In this context, the shape of the tails is determined by the slowest mode $e^{\lambda_i X}$ associated with the leading eigenvalue (i.e., the one with the smallest $|\lambda_i|$), that we label $\lambda_l^{t,b}$ [see ○ in Fig. 4(c)]. Therefore, while the monotonic tail of DW_d around A_t is asymptotically described by $\mathrm{DW}_d(X) - A_t \sim e^{\lambda_{l^+}^t X}$, the oscillatory one around A_b is described by

$$\mathrm{DW}_d(X) - A_b \sim e^{\lambda_{l^-}^b X} = e^{QX}\cos(KX), \tag{12}$$

with $Q = \mathrm{Re}[\lambda_{l^-}^b]$ and $K = \mathrm{Im}[\lambda_{l^-}^b]$.

Close to S_M, the interaction of these DWs can be qualitatively described by the equation,

$$\partial_t D = \varrho e^{QD}\cos(KD) + \nu \equiv F(D), \tag{13}$$

where D is the separation between DWs, $\nu \sim S - S_M$, and ϱ is a positive constant depending on the system parameters [11,68,70,71]. We have to point out that this equation cannot be explicitly derived from our model, and has been included here for illustrating the mechanism of DWs locking.

At S_M ($\nu = 0$) the fixed points of this equation $D_n^s = \frac{\pi}{2K}(2n+1)$, with $n = 0, 1, 2, \ldots$, correspond to the stationary distances at which the locking of DWs occurs [11,68,71]. Figure 4(d) shows these points and their stability using • for stable separations and ○ for unstable ones. If $S \neq S_M$, the stationary separations D_n^s are slightly modified by the factor ν, such that the more we increase the separation ν from S_M, the less LSs form, until eventually no more locking takes place. If the tails are monotonic ($K = 0$), two DWs attract each other until they annihilate one another in a process called coarsening [72]. The DWs studied here [see Fig. 4(c)] exhibit oscillatory tails around A_b, and are behind the formation of the dark LSs shown in Figs. 4(a) and 4(b). In contrast, the tails around A_t

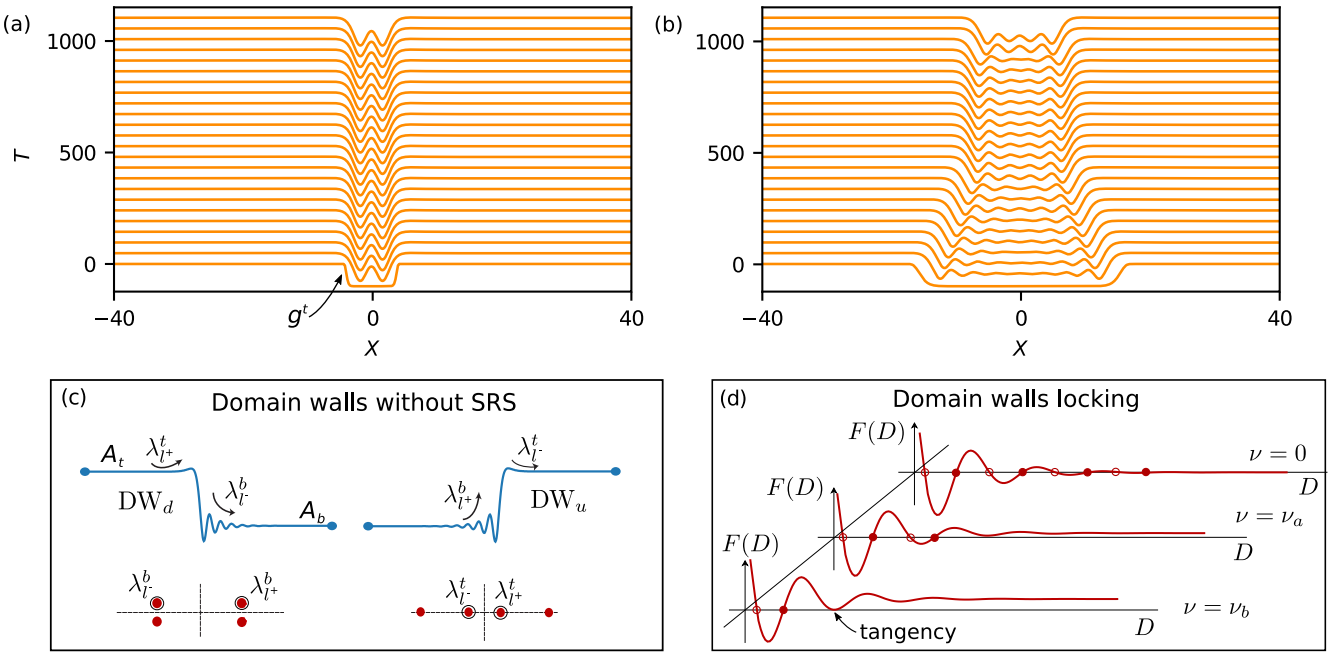

FIG. 4. (a) and (b) The formation of two different dark states starting from two distinct g^t initial conditions. (c) A sketch of the profiles for DW_u and DW_d, and the eigenvalues corresponding to each tail. In (d) we show schematically the function $F(D)$ [see Eq. (13)], defining the DWs locking separations, for three situations: at the Maxwell point ($\nu = 0$), and moving apart from it (ν_a and $\nu_b > \nu_a$).

are monotonic, and they do not lead to the formation of any LS.

B. Bifurcation structure for the dark localized states: Collapsed snaking

The dark LSs formed through this mechanism are organized in a bifurcation diagram like the one shown in Fig. 5, where we plot the L_2 norm,

$$||A||^2 = \frac{1}{l}\int_{-l/2}^{l/2} |A(x)|^2 dx,$$

of the different steady states as a function of S. The red lines correspond to the CW states discussed in Sec. III, and the vertical dashed line marks the Maxwell point S_M. We have computed this diagram fixing $\Delta = 4$, and performing a numerical parameter continuation on S, based on a predictor-corrector method [73,74].

The dark LSs formed through the locking of DWs undergo *collapsed snaking* [25,69,75,76]: Near S_M the LS solution curve [see Fig. 5(a)] oscillates back and forth in S with an amplitude which decreases as descending in $||A||^2$. The labels (i)–(v) correspond to the dark LSs shown on the right. While decreasing $||A||^2$ the LSs broaden as a result of the addition of tail wavelengths, until the DWs reach the domain length. At this stage, the solution curve, which approaches asymptotically S_M, leaves that point and connects back to A_b at MI [see Fig. 3 (top)] [25].

The stability of these states is marked using solid (dashed) lines for stable (unstable) states, and has been obtained by solving the eigenvalue problem,

$$\mathcal{L}\psi = \sigma\psi,$$

where $\mathcal{L} = \mathcal{L}(A)$ is the linear operator associated with the right-hand side of Eq. (3) evaluated at a given LS, and σ and ψ are the eigenvalues and eigenmodes associated with $\mathcal{L}$. We solve this problem numerically, and therefore, $\mathcal{L}$ corresponds to the Jacobian matrix obtained from the spatial discretization of Eq. (3).

This bifurcation structure follows directly from the damped oscillatory DW interaction described by Eq. (13). To understand this correspondence let us relate the sketch shown in Fig. 4(d) and the collapsed snaking of Fig. 5(a). At S_M (i.e., for $\nu = 0$), a number of stable and unstable dark LSs form at the stationary DW separations D_n^s. Thus, the stable (unstable) points in Fig. 4(d) correspond to a set of points on top of the stable (unstable) solution branches at S_M in Fig. 5(a).

When S separates from S_M [see Fig. 4(d) for $\nu = \nu_a$] less stationary separations D_n^s occur, resulting in the disappearance of solution branches corresponding to wider dark LSs. Increasing S further [see Fig. 4(d) for $\nu = \nu_b$], just two intersections occur, and the only remaining solution branches correspond to the stable and unstable single-dip state. Proceeding in this way, eventually no more intersections take place, resulting in the complete disappearance of the LSs. In this picture, the SNs in the collapsed snaking diagram correspond to the tangencies shown in Fig. 4(d). For very large separations (i.e., small $||A||^2$) the interaction is very weak, and wide dark LS branches approach asymptotically S_M.

Dark LSs persist for different values of Δ and undergo temporal oscillatory (i.e., Hopf) instabilities that make them breathe [25]. Figure 5(b) shows the phase diagram of these states in the (Δ, S)-parameter space, where the first two folds of the dark LSs $SN_D^{l,r}$ and the Hopf instability H are plotted. These bifurcation lines bound two regions: (I) where LSs are

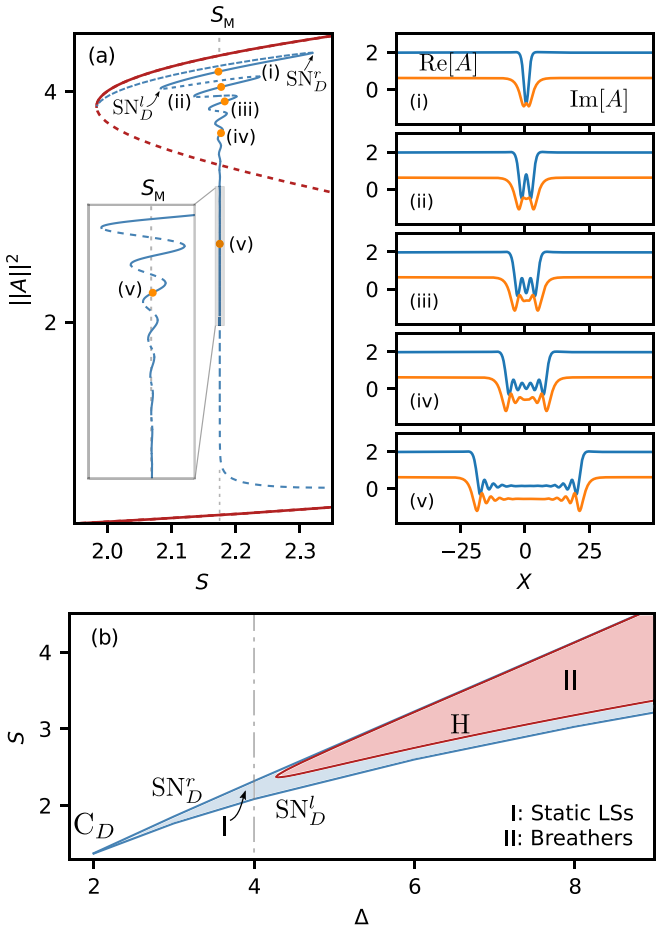

FIG. 5. (a) The collapsed snaking bifurcation diagram for $\Delta = 4$ in the absence of SRS ($f_R = 0$), where the norm $||A||^2$ of the different states is plotted as a function of S. The dark red lines represent the CW state. Stable (unstable) branches are shown with solid (dashed) lines. The labels (i)–(v) correspond to the dark LSs shown on the right. (b) The phase diagram in the (Δ, S)-parameter space with the principal bifurcations lines $\mathrm{SN}_D^{l,r}$, and the Hopf bifurcation H. Regions I and II correspond to static LSs and breathers, respectively.

static, and (II) where LSs exhibit breathing behavior (i.e., localized oscillations).

Increasing Δ, these regions broaden. However, when decreasing Δ they shrink until eventually the different LSs disappear in a sequence of cusp bifurcations [25]. For simplicity here we only plot the cusp C_D associated with the single-dip dark state shown in Fig. 5(i).

V. COEXISTENCE OF BRIGHT AND DARK LOCALIZED STATES IN THE PRESENCE OF STIMULATED RAMAN SCATTERING

The dynamics, interaction, and locking of DWs can be strongly modified by the influence of high-order dispersion effects [33], or long-range interactions [70,71,77–81], such as SRS. Figure 6 shows the temporal evolution of different initial conditions of the form $g^{b,t}$ in the presence of SRS. Figures 6(a) and 6(b) display the evolution of two initial conditions g^t of different widths for $(\Delta, S) = (4, 2.21)$ and $\tau_c = 5$ fs, which lead to the fast formation of two different moving dark LSs. For the same set of parameters, similar dynamical behaviors are observed when considering g^b initial conditions [see Figs. 6(c) and 6(d)]. In this case, the system evolves to two moving bright states of different extensions, which were absent for vanishing SRS.

The formation of these bright states can be also explained in terms of the DWs interaction and locking. Figure 6(e) shows the real part of DW_d and DW_u for the same parameter values used in the previous temporal simulations. Due to the SRS effect, the shape of the tails around either A_t and A_b differs from DW_d to DW_u, and $\mathrm{DW}_u(X) \neq \mathrm{DW}_d(-X)$. A close-up view of the tail of DW_d around A_t [see gray box in Fig. 6(e)] is shown in Fig. 6(f), where we also add the tail of the unperturbed case (i.e., $f_R = 0$) for comparison (see red dashed line). While in the unperturbed case the tail of DW_d leaves A_t monotonically (i.e., the dominant spatial eigenvalue has the form $\lambda_{l^+}^t = +c_1$), in the SRS case the tail leaves A_t in a damped oscillatory manner associated with a complex eigenvalue of the form $\lambda_{l^+}^t = +c_3 + ic_4$. This modification introduces a new way of interaction, such that the locking not only occurs around A_b, but also around A_t, leading to the formation of bright LSs.

In this context, the characteristic time τ_c plays an important role on the modification of the DWs tails: Decreasing τ_c the wavelength of the tails increases, while its decaying weakens. This behavior is captured in Fig. 6(f) where we compare the shape of the tail for $\tau_c = 5$ fs and $\tau_c = 2$ fs. Note that similar tail modifications take place in the presence of other terms breaking X-reflection symmetry such as third-order dispersion [33,35].

Close to the nascent bistability onset (i.e., near $\Delta = \sqrt{3}$), an equation describing the DWs interaction can be derived [43,45]. In that limit, the resulting equation shows that the interaction and DW locking depends on the balance between two factors: (i) a contribution due to the DWs tails, and (ii) a contribution directly related to the long-range interaction (see Eq. (7) in [43]). One could expect that such dependence might persist in the full model (3), with the oscillatory tail contribution being described by Eq. (13). However, the explicit derivation of an interaction equation in the context of the LL model, if possible, might not be straightforward, and it is beyond the scope of the present work.

VI. BIFURCATION STRUCTURE FOR RAMAN DARK AND BRIGHT LOCALIZED STATES

As previously stated in Sec. IV, the collapsed snaking structure is determined by the damped oscillatory nature of the DW tails through Eq. (13). Therefore, any modification of the DW tails and/or features of the interaction law, like the ones induced by the SRS, may change the LS bifurcation structure.

Figure 7(a) shows the modification of the collapsed snaking diagram for $\Delta = 4$ in the presence of SRS when $\tau_c = 5$ fs. The labels (i)–(viii) mark the position of the LSs shown on the right. Due to the $X \to -X$ symmetry breaking these LSs drift at constant speed v and are solutions of Eq. (7).

To compute these states and track them numerically in a given parameter, we need to consider a phase condition of the form $C[A] = 0$ to take account for the LS speed. Here, we define this condition as the constraint $C[A] = d\mathrm{Re}[A]/dX|_{X_0} =$

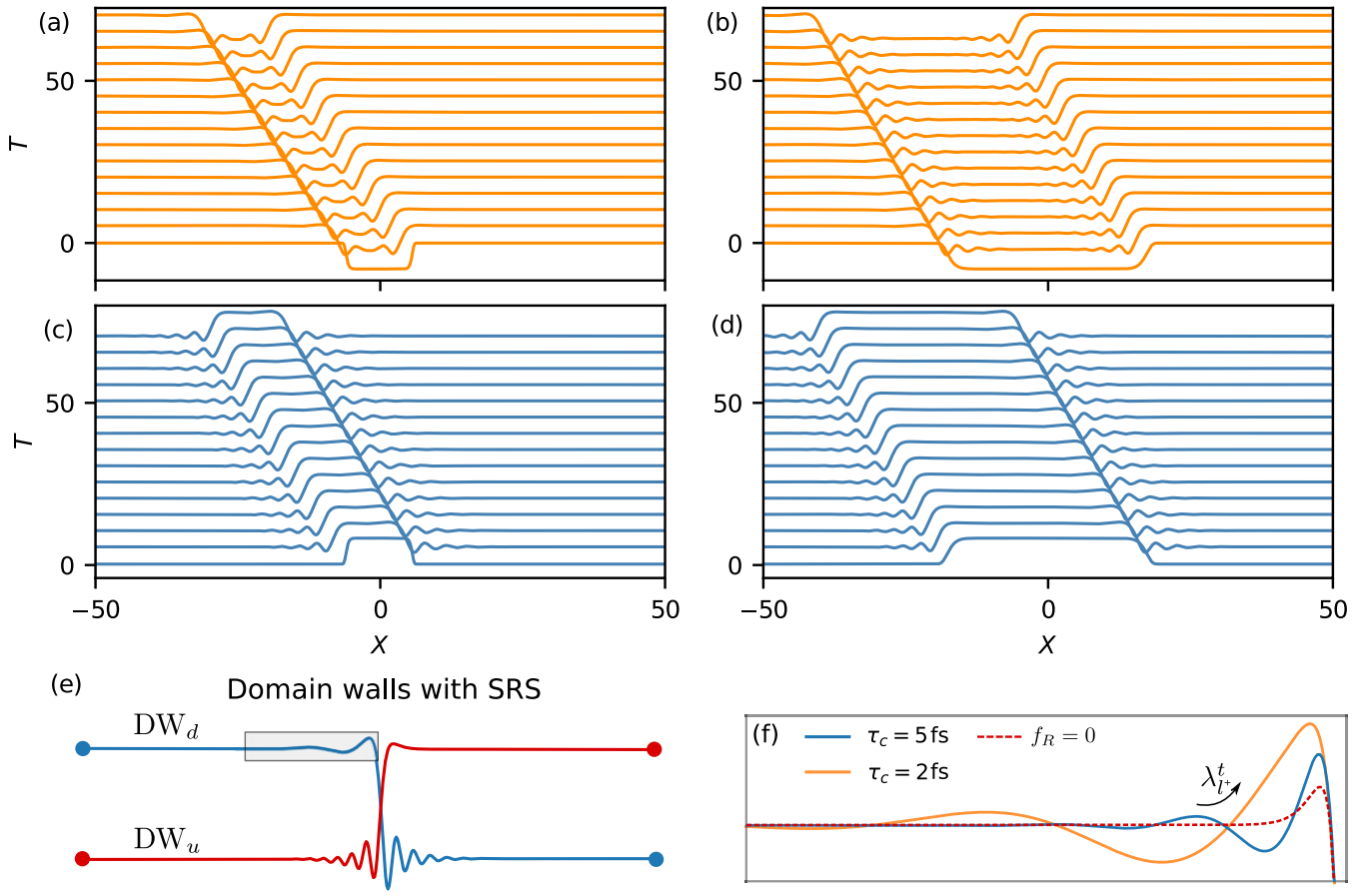

FIG. 6. Formation of LSs in the presence of SRS for $\Delta = 4$, $S = 2.21$, and $\tau_c = 5$ fs. (a) and (b) The formation and temporal evolution of dark LSs starting from two different g^r initial conditions. (c) and (d) The formation and evolution of bright LSs starting from different g^b initial conditions. In (e) we plot schematically two DW profiles corresponding to DW$_d$ and DW$_u$. The gray area highlights the oscillatory tails around A_t, and corresponds to the close-up view shown in (f). For comparison, (f) also shows the tails for $\tau_c = 2$ fs, and in the absence of SRS.

0 which forces one extremum of the LS (maximum or minimum) to be located at $X = X_0$ [32,33]. In this manner, the speed of the LSs is computed as a part of the solution in the continuation algorithm. Figures 7(b) and 7(c) show the computed speed as a function of the LS width D.

The inner subpanels in Fig. 7(a) show a close-up view of the top and bottom part of the bifurcation diagram, which allows us to illustrate better the organization of those solution branches.

The top part of the diagram corresponds to the solution branches associated with the dark LSs presented in Sec. IV. Due to the effect of the SRS, these states are now asymmetric as shown in Figs. 7(i)–7(iv). The irregular form of this part of the diagram may be related to a locking process more complex than the one described in Sec. IV. However, the confirmation of this scenario requires further investigation. The speed v of these states is not constant [see Fig. 7(b)] but oscillates with D, and therefore along the diagram shown in Fig. 7(a). For $D \lesssim 20$, v shows large oscillations with D which correspond to dark states with higher $||A||^2$. For $D \gtrsim 20$ (i.e., decreasing in $||A||^2$), the LSs collapse to the Maxwell point, and so does their speed which saturates to an almost constant value.

The bottom part of the diagram shows a regular collapsed snaking in S, which is absent when $f_R = 0$ [see Fig. 5(a)]. This new bifurcation structure is related to the locking of DWs around A_t, which is now possible due to the presence of oscillatory tails about such state, and the presence of the long-range interaction (see Sec. V) [43,45]. Four representative LS examples along this part of the diagram are shown in Figs. 7(v)–7(viii). These asymmetric bright LSs drift at constant speed, whose damped oscillatory dependence with D is plotted Fig. 7(c).

The bifurcation structure shown in Fig. 7(a) is different from the one obtained in the framework of the reduced real parameter equation around $\Delta = \sqrt{3}$ [45]. While in the former case the solution curve approaches asymptotically the Maxwell point in an oscillatory fashion (i.e., undergo collapsed snaking), in the latter, the approaching is monotonous, due to the absence of oscillatory tails on the DWs profiles [45]. Furthermore, the morphological differences between the top and bottom parts of the diagram shown in Fig. 7(a), fade away in the description performed around $\Delta = \sqrt{3}$, where bright and dark states undergo the same bifurcation structure.

Dark and bright LSs persist for different values of Δ as shown in the (Δ, S)-phase diagram of Fig. 8 for $\tau_c = 5$ fs. This diagram has been computed through a two-parameter continuation in (Δ, S) of the main bifurcations of system: the first two folds $\mathrm{SN}_D^{l,r}$ of the single-dip dark LS, the first two folds $\mathrm{SN}_B^{l,r}$ of the single-peak bright LS, and the Hopf

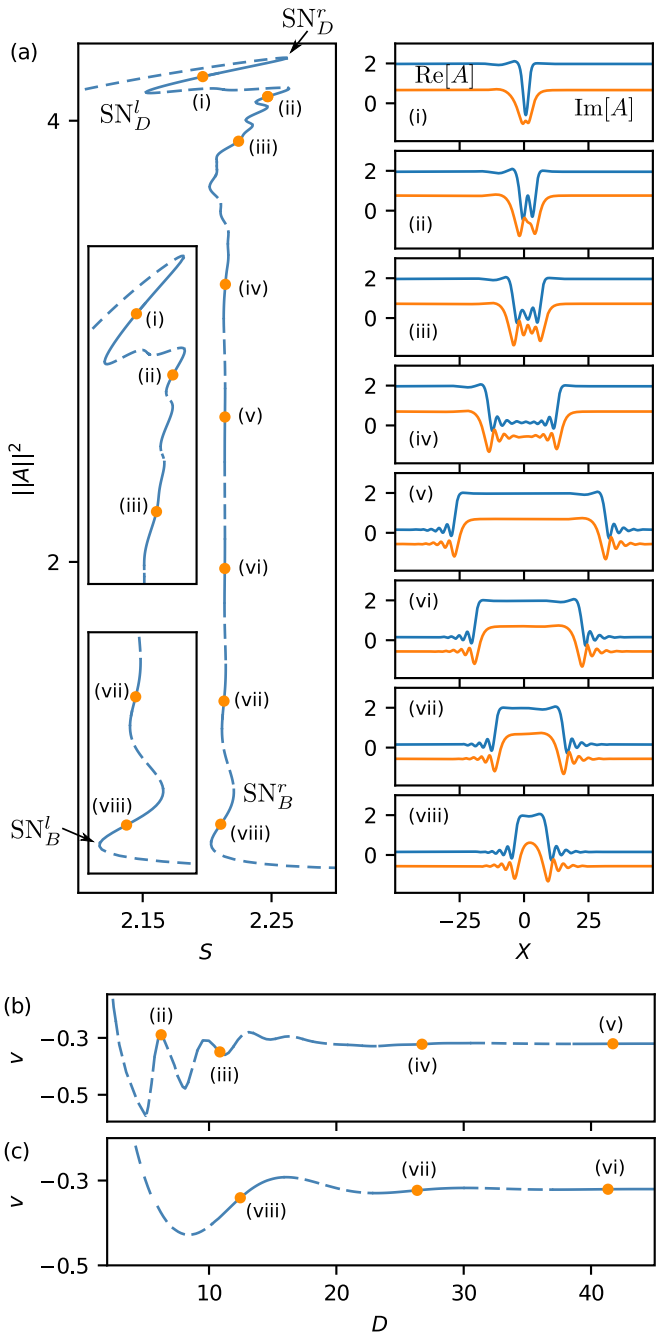

FIG. 7. (a) The LSs bifurcation diagram for $\Delta = 4$ in the presence of SRS for $\tau_c = 5$ fs. The labels (i)–(viii) correspond to the LSs shown on the right. Stable (unstable) solution branches are marked using solid (dashed) lines. (b) The speed v of the dark LSs as a function of their width D. In (c) the same as in (b) for bright LSs.

bifurcation H. The dashed gray lines correspond to $SN_D^{l,r}$ in the absence of SRS (i.e., $f_R = 0$), the vertical pointed-dashed line to the bifurcation diagram shown in Fig. 7(a) for $\Delta = 4$, and the dashed one to Fig. 9 ($\Delta = 5$).

In the presence of SRS, the different dynamical regions shown in Fig. 5(b), such as the region of existence of single-dip dark LSs (i.e., region I) and the breathing region (i.e., region II) shrink, leading to a partial stabilization of the breathing dark states.

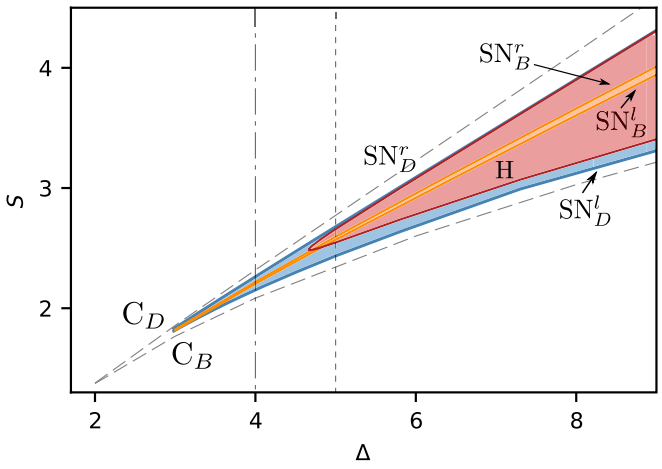

FIG. 8. Phase diagram in the (Δ, S)-parameter space showing the main bifurcation lines of the system in the presence of SRS ($f_R \neq 0$) for $\tau_c = 5$ fs: $SN_D^{l,r}$ are the first two folds of the dark states, $SN_B^{l,r}$ are the first two folds of the bright LSs, and H corresponds to the Hopf bifurcation. The dashed gray lines correspond to $SN_D^{l,r}$ in the absence of SRS, and vertical point-dashed and dashed vertical ones to the bifurcation diagrams shown in Figs. 7(a) and 9, respectively.

The area in-between $SN_B^{l,r}$ shows the region of existence of the bright LSs, which widens increasing Δ. Decreasing Δ, however, this region shrinks until eventually SN_B^l and SN_B^r collide and disappear in a cusp bifurcation C_B.

The collapsed snaking structure is preserved for larger values of Δ, as shown in Fig. 9 for $\Delta = 5$. Here, the bottom part of the diagram is very much like the one shown in Fig. 7(a), and some representative examples of bright LSs are shown in Figs. 9(i)–9(iv). However, the top part of the diagram, undergoes a Hopf instability (see close-up view in Fig. 9), that makes the single-dip dark state [see profile (vi)] breathe as shown in Fig. 9(vii).

Bright LSs may also undergo oscillatory instabilities [44], however, for the range of parameters studied in this work, we have not observed such type of dynamics.

VII. INFLUENCE OF τ_c ON THE LOCALIZED STATE DYNAMICS AND STABILITY

So far we have studied the influence of the SRS on the dynamics and stability of LSs for a single value of the characteristic time $\tau_c = 5$ fs. This parameter strongly impacts the stability of LSs as shown in the context of anomalous dispersion [40], and one may wonder how the previous scenario modifies when varying its value.

To clarify this point we perform a two-parameter continuation of the main bifurcations of the system in S and τ_c by fixing Δ. The outcome of this computation is shown in Fig. 10 for two different values of Δ. In Fig. 10(a) we show the (τ_c, S)-phase diagram for $\Delta = 5$, and Fig. 10(b) shows the one for $\Delta = 4$. In both cases the horizontal dashed lines mark the position of $SN_D^{l,r}$ in the absence of SRS for comparison. Note that the Hopf bifurcation H is present for $\Delta = 5$ [see Fig. 10(a)], while absent for $\Delta = 4$ [see Fig. 10(b)].

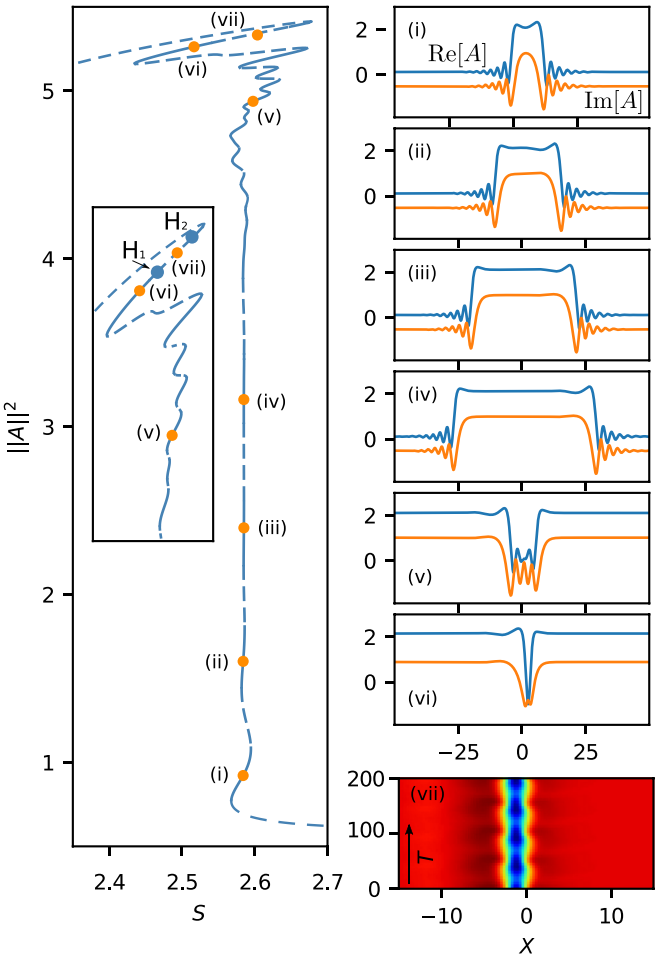

FIG. 9. Collapsed snaking for $\Delta = 5$ and $\tau_c = 5$ fs corresponding to the dashed vertical line shown in Fig. 8. The labels (i)–(vi) correspond to the asymmetric LSs shown on the right, and panel (vii) shows the time evolution of a breather within several oscillatory periods.

For $\Delta = 5$, the modification of the collapsed snaking structure with τ_c is depicted in Fig. 11 for three particular values of τ_c corresponding to the vertical dashed lines shown in Fig. 10(a). For $\tau_c = 10$ fs [see Fig. 11(a)] the scenario is very similar to the unperturbed case (see gray diagram computed for $f_R = 0$), although the Hopf instability slightly modifies its position as shown in the close-up view of Fig. 11(a). In addition, the collapsed snaking corresponding to the bottom of the diagram is strongly compressed. Increasing τ_c further, the Raman response function R becomes sharper and highly damped (see Sec. II) tending to an almost instantaneous response, and therefore, the deviation from the unperturbed case is almost negligible.

Reducing τ_c, however, the SRS modifies strongly the DW tails (see Sec. V), and as a consequence the LS bifurcation structure. Thus, while the region of existence of dark LSs and breathers shrinks, the region of existence of bright LSs broadens [see phase diagram in Fig. 10(a)]. An example of this situation is shown in Fig. 11(b) for $\tau_c = 5$ fs, where, whereas the top part of the diagram is highly modified (see close-up view), the bottom one shows larger damped oscillations in S

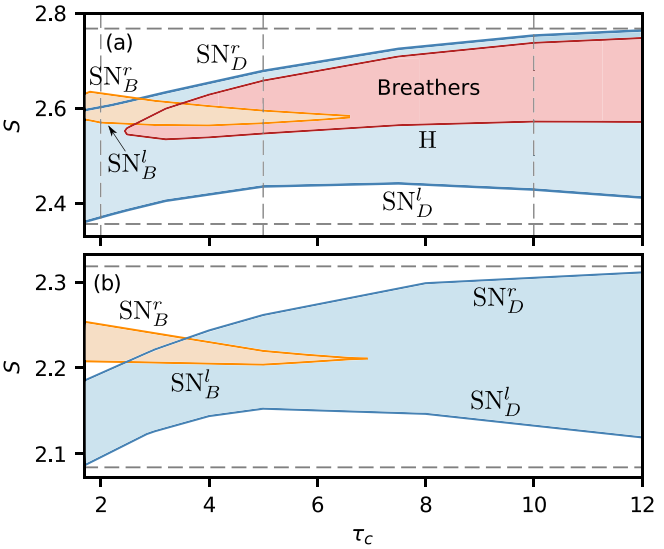

FIG. 10. (a) The (τ_c, S)-phase diagram for $\Delta = 5$, where the main bifurcations of the system are plotted: $SN_D^{l,r}$ are the first two fold of the dark states, $SN_B^{l,r}$ are the first two folds of the bright LSs, and H represents the Hopf bifurcation. The vertical lines in (a) correspond to the bifurcation diagrams shown in Fig. 11. (b) The same type of phase diagram for $\Delta = 4$. In both panels horizontal dashed lines represent the position of $SN_D^{l,r}$ for vanishing SRS.

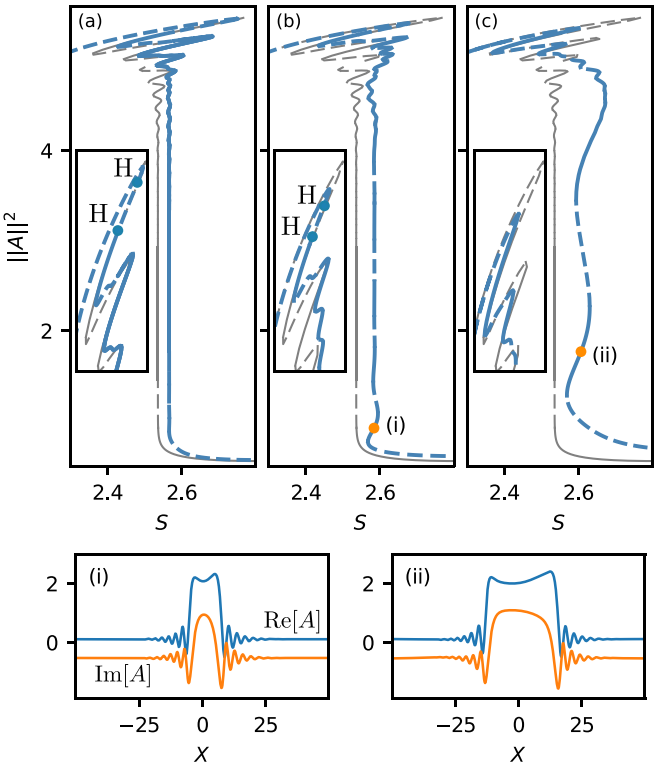

FIG. 11. Modification of the collapsed snaking structure for $\Delta = 5$ while decreasing τ_c (see solid blue diagram): In (a) $\tau_c = 10$ fs, in (b) $\tau_c = 5$ fs, and in (c) $\tau_c = 2$ fs. In gray we have also plotted the diagram in the absence of SRS for comparison. The inset panels show a close-up view of the top part of the collapsed snaking where the Hopf instabilities H are signaled. Two examples of bright LS profiles are plotted in subpanels (i) and (ii).

as a result of the appearance of bright LSs like the one shown in Fig. 11(i).

Decreasing τ_c even further, the Hopf bifurcation disappears, and with it, the breathing behavior [see Fig. 10(a)], leading to the stabilization of the single-dip dark states. In this regime the bifurcation structure is similar to the one depicted in Fig. 11(c) for $\tau_c = 2$ fs. For this value of τ_c the branches corresponding to the dark states are strongly modified [see the detailed view in the inset of panel 11(c)], and the bright LSs increase their region of existence due to the dominant interaction of the DW tails around A_t. An example of this type of bright LSs is shown in Fig. 11(ii). For $\Delta = 4$ [see Fig. 10(b)] the scenario is quite similar to the previous one, despite of the absence of the breather regime.

VIII. DISCUSSION AND CONCLUSIONS

The stimulated Raman scattering (SRS), also known as the Raman effect, has important implications on the dynamics and stability of LSs arising in nonlinear dispersive cavities made of amorphous materials, such as fiber cavities. Although several studies have addressed this problem in both anomalous and normal dispersion regimes [36–45], a systematic and detailed bifurcation analysis was lacking.

In this paper, we have unveiled the implications that SRS has on the bifurcation structure of LSs in the normal group velocity dispersion regime. To do so, we have used the mean-field Lugiato-Lefever equation, with a Raman response term, which describes Kerr dispersive cavities in a high finesse limit (see Sec. II).

In the absence of SRS, the typical LSs arising in the normal regime are dark. These type of LSs form due to the locking of DWs which exist within a region of bistability between two different CW states. The locking occurs through the overlapping of the DW tails, leading to LSs of different extensions that can be seen as a portion of one CW state embedded on the other one (see Secs. III and IV). From a bifurcation perspective, these states undergo *collapsed snaking* (see Sec. IV): The LS solution curve experiences a sequence of exponentially decaying oscillations in the pump S around the Maxwell point of the system, as a result of the DW interaction and locking [25,26,69]. For large values of detuning Δ, moreover, these states undergo oscillatory instabilities that make them breathe [25,26].

The presence of SRS strongly modifies the dynamics and stability of the previous states, and furthermore induces the emergence of bright LSs [43]. From a dynamical point of view, the SRS effect has two main implications. First, the SRS term breaks the reflection symmetry $X \to -X$, inducing a constant drift in the, otherwise static, LSs. Second, the SRS modifies the spatial eigenvalues of the CW states (i.e., the shape of the DWs oscillatory tails), and the interaction and locking of DWs. As a result, the dark states modify their dynamics, and bright LSs arise (see Sec. V).

Dark and bright Raman LSs undergo collapsed snaking that we have characterized in detail as a function of Δ and S for a fixed value of the characteristic time parameter τ_c. Figure 8 in Sec. VI summarizes the main dynamical regimes in the (Δ, S)-phase space for $\tau = 5$ fs. As shown in [40,43], the parameter τ_c has important implications regarding the LS stability. These implications have been analyzed in detail in Sec. VII, and the main results are summarized in Fig. 10. The larger the value of τ_c, the stronger the SRS effect, and the modification of the DW tails, resulting in a more complex collapsed snaking structure (see Fig. 11).

Note that $\tau_c = \sqrt{L|\beta_2|/2\alpha}$, and we can reinterpret the previous results in terms of the cavity length L, losses α, and chromatic dispersion coefficient β_2. Thus, if we fix L and α, $\tau_c \propto \sqrt{|\beta_2|}$, and we can reformulate the conclusions of Sec. VII in terms of β_2: Increasing β_2 the existence region of dark LSs and breathers widens, while the one of bright LSs shrinks, and eventually disappears. Some physical parameter values of all fiber cavities, for which the observation of these types of structures may be possible, are presented in [43].

A similar scenario, also supported experimentally, can be found when the X-reflection symmetry is broken through third-order chromatic dispersion [33,82]. In such case, the modification of the DW tails about A_b is much more prominent than in the presence of SRS, and therefore the existence region of bright LSs is much wider. Furthermore, the extension of this region increases with the strength of the third-order dispersion, in contrast to the SRS case where it decreases with τ_c.

This work has been performed for a fixed domain length $l = 100$, although the results presented here can be generalized to different domain extensions. As the LS width is an integer multiple of the DW tails wavelength, the size of the domain can strongly constraint the variety of LSs allowed in the system. Thus, the larger the domain (i.e., the cavity), the wider the states that can emerge in the system.

The final aim of studies of this kind is to be useful for understanding the formation and dynamics of LSs in Kerr nonlinear optical cavities, and guiding experiments in this type of system, as has been done previously [20,82].

ACKNOWLEDGMENTS

P.P.-R. and M.T. acknowledge support from the Fonds National de la Recherche Scientifique F.R.S.-FNRS (Belgium). S.C. acknowledges the LABEX CEMPI (ANR-11-LABX-0007) as well as the Ministry of Higher Education and Research, Hauts de France council, and European Regional Development Fund (ERDF) through the Contract de Projets Etat-Region (CPER Photonics for Society P4S). M.G.C. acknowledges funding from Millennium Institute for Research in Optics (MIRO) and FONDECYT Project No. 1180903.

[1] G. Nicolis and I. Prigogine, *Self-Organization in Nonequilibrium Systems: From Dissipative Structures to Order Through Fluctuations* (Wiley, New York, 1977).

[2] M. C. Cross and P. C. Hohenberg, Pattern formation outside of equilibrium, Rev. Mod. Phys. **65**, 851 (1993).

[3] N. Akhmediev and A. Ankiewicz (eds.), *Dissipative Solitons*, Lecture Notes in Physics (Springer-Verlag, Berlin/Heidelberg, 2005).

[4] N. Akhmediev and A. Ankiewicz, *Dissipative Solitons: From Optics to Biology and Medicine*, Lecture Notes in Physics (Springer-Verlag, Berlin/Heidelberg, 2008).

[5] O. Descalzi, M. G. Clerc, S. Residori, and G. Assanto (eds.), *Localized States in Physics: Solitons and Patterns* (Springer-Verlag, Berlin/Heidelberg, 2011).

[6] Y. K. Chembo, D. Gomila, M. Tlidi, and C. R. Menyuk, Theory and applications of the Lugiato-Lefever equation, Eur. Phys. J. D **71**, 299 (2017).

[7] M. Tlidi, M. G. Clerc, and K. Panajotov, Dissipative structures in matter out of equilibrium: From chemistry, photonics and biology, the legacy of Ilya Prigogine (part 2), Philos. Trans. R. Soc., A **376**, 20180276 (2018).

[8] M. Tlidi, M. G. Clerc, and K. Panajotov, Dissipative structures in matter out of equilibrium: From chemistry, photonics and biology, the legacy of Ilya Prigogine (part 1), Philos. Trans. R. Soc., A **376**, 20180114 (2018).

[9] B. A. Malomed and D. Mihalache, Nonlinear waves in optical and matter-wave media: A topical survey of recent theoretical and experimental results, Rom. J. Phys **64**, 106 (2019).

[10] L. Lugiato, F. Prati, M. Gorodetsky, and T. Kippenberg, From the Lugiato-Lefever equation to microresonator-based soliton Kerr frequency combs, Philos. Trans. R. Soc., A **376**, 20180113 (2018).

[11] P. Coullet, Localized patterns and fronts in nonequilibrium systems, Int. J. Bifurcation Chaos **12**, 2445 (2002).

[12] A. J. Scroggie, W. J. Firth, G. S. McDonald, M. Tlidi, R. Lefever, and L. A. Lugiato, Pattern formation in a passive Kerr cavity, Chaos, Solitons & Fractals **4**, 1323 (1994).

[13] W. J. Firth and A. Lord, Two-dimensional solitons in a Kerr cavity, J. Mod. Opt. **43**, 1071 (1996).

[14] W. J. Firth, G. K. Harkness, A. Lord, J. M. McSloy, D. Gomila, and P. Colet, Dynamical properties of two-dimensional Kerr cavity solitons, J. Opt. Soc. Am. B **19**, 747 (2002).

[15] D. Gomila, M. A. Matías, and P. Colet, Excitability Mediated by Localized Structures in a Dissipative Nonlinear Optical Cavity, Phys. Rev. Lett. **94**, 063905 (2005).

[16] F. Leo, S. Coen, P. Kockaert, S.-P. Gorza, P. Emplit, and M. Haelterman, Temporal cavity solitons in one-dimensional Kerr media as bits in an all-optical buffer, Nat. Photonics **4**, 471 (2010).

[17] F. Leo, L. Gelens, P. Emplit, M. Haelterman, and S. Coen, Dynamics of one-dimensional Kerr cavity solitons, Opt. Express **21**, 9180 (2013).

[18] T. Herr, V. Brasch, J. D. Jost, C. Y. Wang, N. M. Kondratiev, M. L. Gorodetsky, and T. J. Kippenberg, Temporal solitons in optical microresonators, Nat. Photonics **8**, 145 (2014).

[19] X. Xue, Y. Xuan, Y. Liu, P.-H. Wang, S. Chen, J. Wang, D. E. Leaird, M. Qi, and A. M. Weiner, Mode-locked dark pulse Kerr combs in normal-dispersion microresonators, Nat. Photonics **9**, 594 (2015).

[20] B. Garbin, Y. Wang, S. G. Murdoch, G.-L. Oppo, S. Coen, and M. Erkintalo, Experimental and numerical investigations of switching wave dynamics in a normally dispersive fibre ring resonator, Eur. Phys. J. D **71**, 240 (2017).

[21] P. Del'Haye, A. Schliesser, O. Arcizet, T. Wilken, R. Holzwarth, and T. J. Kippenberg, Optical frequency comb generation from a monolithic microresonator, Nature (London) **450**, 1214 (2007).

[22] T. J. Kippenberg, R. Holzwarth, and S. A. Diddams, Microresonator-based optical frequency combs, Science **332**, 555 (2011).

[23] A. Pasquazi, M. Peccianti, L. Razzari, D. J. Moss, S. Coen, M. Erkintalo, Y. K. Chembo, T. Hansson, S. Wabnitz, P. Del'Haye, X. Xue, A. M. Weiner, and R. Morandotti, Micro-combs: A novel generation of optical sources, Phys. Rep. **729**, 1 (2018).

[24] S. Coen, M. Tlidi, P. Emplit, and M. Haelterman, Convection versus Dispersion in Optical Bistability, Phys. Rev. Lett. **83**, 2328 (1999).

[25] P. Parra-Rivas, E. Knobloch, D. Gomila, and L. Gelens, Dark solitons in the Lugiato-Lefever equation with normal dispersion, Phys. Rev. A **93**, 063839 (2016).

[26] P. Parra-Rivas, D. Gomila, E. Knobloch, S. Coen, and L. Gelens, Origin and stability of dark pulse Kerr combs in normal dispersion resonators, Opt. Lett. **41**, 2402 (2016).

[27] D. Gomila, A. J. Scroggie, and W. J. Firth, Bifurcation structure of dissipative solitons, Physica D **227**, 70 (2007).

[28] P. Parra-Rivas, D. Gomila, L. Gelens, and E. Knobloch, Bifurcation structure of localized states in the Lugiato-Lefever equation with anomalous dispersion, Phys. Rev. E **97**, 042204 (2018).

[29] P. Parra-Rivas, D. Gomila, M. A. Matías, S. Coen, and L. Gelens, Dynamics of localized and patterned structures in the Lugiato-Lefever equation determine the stability and shape of optical frequency combs, Phys. Rev. A **89**, 043813 (2014).

[30] M. Tlidi and L. Gelens, High-order dispersion stabilizes dark dissipative solitons in all-fiber cavities, Opt. Lett. **35**, 306 (2010).

[31] M. Tlidi, L. Bahloul, L. Cherbi, A. Hariz, and S. Coulibaly, Drift of dark cavity solitons in a photonic-crystal fiber resonator, Phys. Rev. A **88**, 035802 (2013).

[32] P. Parra-Rivas, D. Gomila, F. Leo, S. Coen, and L. Gelens, Third-order chromatic dispersion stabilizes Kerr frequency combs, Opt. Lett. **39**, 2971 (2014).

[33] P. Parra-Rivas, D. Gomila, and L. Gelens, Coexistence of stable dark- and bright-soliton Kerr combs in normal-dispersion resonators, Phys. Rev. A **95**, 053863 (2017).

[34] V. E. Lobanov, A. V. Cherenkov, A. E. Shitikov, I. A. Bilenko, and M. L. Gorodetsky, Dynamics of platicons due to third-order dispersion, Eur. Phys. J. D **71**, 185 (2017).

[35] J. H. Talla Mbé, C. Milián, and Y. K. Chembo, Existence and switching behavior of bright and dark Kerr solitons in whispering-gallery mode resonators with zero group-velocity dispersion, Eur. Phys. J. D **71**, 196 (2017).

[36] C. Milián, A. V. Gorbach, M. Taki, A. V. Yulin, and D. V. Skryabin, Solitons and frequency combs in silica microring resonators: Interplay of the Raman and higher-order dispersion effects, Phys. Rev. A **92**, 033851 (2015).

[37] Y. K. Chembo, I. S. Grudinin, and N. Yu, Spatiotemporal dynamics of Kerr-Raman optical frequency combs, Phys. Rev. A **92**, 043818 (2015).

[38] V. E. Lobanov, G. Lihachev, T. J. Kippenberg, and M. L. Gorodetsky, Frequency combs and platicons in optical microresonators with normal GVD, Opt. Express **23**, 7713 (2015).

[39] X. Yi, Q.-F. Yang, K. Y. Yang, and K. Vahala, Theory and measurement of the soliton self-frequency shift and efficiency in optical microcavities, Opt. Lett. **41**, 3419 (2016).

[40] Y. Wang, M. Anderson, S. Coen, S. G. Murdoch, and M. Erkintalo, Stimulated Raman Scattering Imposes Fundamental Limits to the Duration and Bandwidth of Temporal Cavity Solitons, Phys. Rev. Lett. **120**, 053902 (2018).

[41] W. Chen, B. Garbin, A. U. Nielsen, S. Coen, S. G. Murdoch, and M. Erkintalo, Experimental observations of breathing Kerr temporal cavity solitons at large detunings, Opt. Lett. **43**, 3674 (2018).

[42] A. V. Cherenkov, N. M. Kondratiev, V. E. Lobanov, A. E. Shitikov, D. V. Skryabin, and M. L. Gorodetsky, Raman-Kerr frequency combs in microresonators with normal dispersion, Opt. Express **25**, 31148 (2017).

[43] M. G. Clerc, S. Coulibaly, and M. Tlidi, Time-delayed nonlocal response inducing traveling temporal localized structures, Phys. Rev. Research **2**, 013024 (2020).

[44] S. Yao, C. Bao, P. Wang, and C. Yang, Generation of stable and breathing flat-top solitons via Raman assisted four wave mixing in microresonators, Phys. Rev. A **101**, 023833 (2020).

[45] M. G. Clerc, S. Coulibaly, P. Parra-Rivas, and M. Tlidi, Nonlocal Raman response in Kerr resonators: Moving temporal localized structures and bifurcation structure, Chaos **30**, 083111 (2020).

[46] L. A. Lugiato and R. Lefever, Spatial Dissipative Structures in Passive Optical Systems, Phys. Rev. Lett. **58**, 2209 (1987).

[47] M. Haelterman, S. Trillo, and S. Wabnitz, Dissipative modulation instability in a nonlinear dispersive ring cavity, Opt. Commun. **91**, 401 (1992).

[48] Q. Lin and G. P. Agrawal, Raman response function for silica fibers, Opt. Lett. **31**, 3086 (2006).

[49] Y. K. Chembo and C. R. Menyuk, Spatiotemporal Lugiato-Lefever formalism for Kerr-comb generation in whispering-gallery-mode resonators, Phys. Rev. A **87**, 053852 (2013).

[50] P. Kockaert, P. Tassin, G. Van der Sande, I. Veretennicoff, and M. Tlidi, Negative diffraction pattern dynamics in nonlinear cavities with left-handed materials, Phys. Rev. A **74**, 033822 (2006).

[51] Z. Ziani, G. Lévêque, A. Akjouj, S. Coulibaly, and A. Taki, Characterization of spatiotemporal chaos in arrays of nonlinear plasmonic nanoparticles, Phys. Rev. B **100**, 165423 (2019).

[52] U. Peschel, O. Egorov, and F. Lederer, Discrete cavity solitons, in *Nonlinear Guided Waves and their Applications* (Optical Society of America, Washington, DC, 2004), p. WB6.

[53] J. Cuevas-Maraver, P. G. Kevrekidis, and F. Williams, The sine-Gordon model and its applications, in *Nonlinear Systems and Complexity* (Springer, Cham, 2014).

[54] D. Gomila and P. Colet, Transition from hexagons to optical turbulence, Phys. Rev. A **68**, 011801(R) (2003).

[55] D. Gomila and P. Colet, Fluctuations and correlations in hexagonal optical patterns, Phys. Rev. E **66**, 046223 (2002).

[56] N. Périnet, N. Verschueren, and S. Coulibaly, Eckhaus instability in the Lugiato-Lefever model, Eur. Phys. J. D **71**, 243 (2017).

[57] C. Godey, I. V. Balakireva, A. Coillet, and Y. K. Chembo, Stability analysis of the spatiotemporal Lugiato-Lefever model for Kerr optical frequency combs in the anomalous and normal dispersion regimes, Phys. Rev. A **89**, 063814 (2014).

[58] P. Parra-Rivas, D. Gomila, P. Colet, and L. Gelens, Interaction of solitons and the formation of bound states in the generalized Lugiato-Lefever equation, Eur. Phys. J. D **71**, 198 (2017).

[59] A. G. Vladimirov, S. V. Gurevich, and M. Tlidi, Effect of Cherenkov radiation on localized-state interaction, Phys. Rev. A **97**, 013816 (2018).

[60] M. Anderson, F. Leo, S. Coen, M. Erkintalo, and S. G. Murdoch, Observations of spatiotemporal instabilities of temporal cavity solitons, Optica **3**, 1071 (2016).

[61] Z. Liu, M. Ouali, S. Coulibaly, M. Clerc, M. Taki, and M. Tlidi, Characterization of spatiotemporal chaos in a Kerr optical frequency comb and in all fiber cavities, Opt. Lett. **42**, 1063 (2017).

[62] K. Panajotov, M. G. Clerc, and M. Tlidi, Spatiotemporal chaos and two-dimensional dissipative rogue waves in Lugiato-Lefever model, Eur. Phys. J. D **71**, 176 (2017).

[63] K. Panajotov, M. Tlidi, Y. Song, and H. Zhang, Control of dissipative rogue waves in nonlinear cavity optics: Optical injection and time-delayed feedback, Chaos **30**, 053103 (2020).

[64] M. Tlidi and K. Panajotov, Two-dimensional dissipative rogue waves due to time-delayed feedback in cavity nonlinear optics, Chaos **27**, 013119 (2017).

[65] A. Coillet, J. Dudley, G. Genty, L. Larger, and Y. K. Chembo, Optical rogue waves in whispering-gallery-mode resonators, Phys. Rev. A **89**, 013835 (2014).

[66] G. Agrawal, *Applications of Nonlinear Fiber Optics* (Academic Press, Cambridge, 2008).

[67] J. M. Chomaz, Absolute and Convective Instabilities in Nonlinear Systems, Phys. Rev. Lett. **69**, 1931 (1992).

[68] P. Coullet, C. Elphick, and D. Repaux, Nature of Spatial Chaos, Phys. Rev. Lett. **58**, 431 (1987).

[69] P. Parra-Rivas, L. Gelens, and F. Leo, Localized structures in dispersive and doubly resonant optical parametric oscillators, Phys. Rev. E **100**, 032219 (2019).

[70] M. G. Clerc, D. Escaff, and V. M. Kenkre, Analytical studies of fronts, colonies, and patterns: Combination of the Allee effect and nonlocal competition interactions, Phys. Rev. E **82**, 036210 (2010).

[71] M. G. Clerc, D. Escaff, and V. M. Kenkre, Patterns and localized structures in population dynamics, Phys. Rev. E **72**, 056217 (2005).

[72] S. M. Allen and J. W. Cahn, A microscopic theory for antiphase boundary motion and its application to antiphase domain coarsening, Acta Metall. **27**, 1085 (1979).

[73] E. Doedel, H. B. Keller, and J. P. Kernevez, Numerical analysis and control of bifurcation problems (ii): bifurcation in infinite dimensions, Int. J. Bifurcation Chaos **01**, 745 (1991).

[74] E. Doedel, H. B. Keller, and J. P. Kernevez, Numerical analysis and control of bifurcation problems (i): bifurcation in finite dimensions, Int. J. Bifurcation Chaos **01**, 493 (1991).

[75] J. Knobloch and T. Wagenknecht, Homoclinic snaking near a heteroclinic cycle in reversible systems, Physica D **206**, 82 (2005).

[76] A. Yochelis, J. Burke, and E. Knobloch, Reciprocal Oscillons and Nonmonotonic Fronts in Forced Nonequilibrium Systems, Phys. Rev. Lett. **97**, 254501 (2006).

[77] D. Escaff, Non-local defect interaction in one dimension: Weak versus strong non-locality, Eur. Phys. J. D **62**, 33 (2011).

[78] P. Colet, M. A. Matías, L. Gelens, and D. Gomila, Formation of localized structures in bistable systems through nonlocal

spatial coupling. I. General framework, Phys. Rev. E **89**, 012914 (2014).

[79] L. Gelens, M. A. Matías, D. Gomila, T. Dorissen, and P. Colet, Formation of localized structures in bistable systems through nonlocal spatial coupling. II. The nonlocal Ginzburg-Landau equation, Phys. Rev. E **89**, 012915 (2014).

[80] C. Fernandez-Oto, M. Tlidi, D. Escaff, and M. G. Clerc, Strong interaction between plants induces circular barren patches: Fairy circles, Philos. Trans. R. Soc., A **372**, 20140009 (2014).

[81] D. Escaff, C. Fernandez-Oto, M. G. Clerc, and M. Tlidi, Localized vegetation patterns, fairy circles, and localized patches in arid landscapes, Phys. Rev. E **91**, 022924 (2015).

[82] Z. Li, Z. Li, Y. Xu, Y. Xu, S. Coen, S. Coen, S. G. Murdoch, S. G. Murdoch, M. Erkintalo, and M. Erkintalo, Experimental observations of bright dissipative cavity solitons and their collapsed snaking in a Kerr resonator with normal dispersion driving, Optica **7**, 1195 (2020).